

Active Control of Mode Crossover and Mode Hopping of Spin Waves in a Ferromagnetic Antidot Lattice


Samiran Choudhury,¹ Sudip Majumder,¹ Saswati Barman,^{1,2} YoshiChika Otani,^{3,4} and Anjan Barman^{1,*}

¹*Department of Condensed Matter Physics and Material Sciences, S. N. Bose National Centre for Basic Sciences, Block JD, Sector III, Salt Lake, Kolkata 700 106, India*

²*Institute of Engineering and Management, Sector V, Salt Lake, Kolkata 700 091, India*

³*Institute for Solid State Physics, University of Tokyo, 5-1-5 Kashiwanoha, Kashiwa, Chiba 277-8581, Japan*

⁴*RIKEN-CEMS, 2-1 Hirosawa, Wako, Saitama 351-0198, Japan*

 (Received 22 July 2018; revised manuscript received 29 October 2018; published 18 December 2018)

Active control of spin-wave dynamics is demonstrated using broadband ferromagnetic resonance in two-dimensional $\text{Ni}_{80}\text{Fe}_{20}$ antidot lattices arranged in a hexagonal lattice with fixed lattice constant, but varying antidot diameter. A strong modification in the spin-wave spectra is obtained with the variation in the antidot diameter as well as with the strength and orientation of the bias magnetic field. A broad band of modes is observed for the lattice with the higher antidot diameter, which decreases systematically as the antidot diameter is reduced. A crossover between the higher-frequency branches is achieved in lattices with higher antidot diameters. In addition, the spin-wave modes in all lattices show a strong six-fold anisotropic behavior due to the variation of internal field distribution as a function of the bias-field orientation. A mode-hopping-like behavior is observed in the angular dispersions of spin-wave spectra for samples having intermediate hole diameters. Micromagnetic simulations qualitatively reproduce the experimentally observed spin-wave modes and the simulated mode profiles reveal the presence of extended and quantized standing spin-wave modes in these lattices. These observations are significant for large tunability and anisotropic propagation of spin waves in GHz-frequency magnetic devices.

DOI: [10.1103/PhysRevApplied.10.064044](https://doi.org/10.1103/PhysRevApplied.10.064044)

I. INTRODUCTION

Ferromagnetic (FM) antidot (AD) (hole) lattices (ADLs) [1], i.e., periodically arranged holes embedded in a FM thin film, are artificial crystals, which are fabricated by structuring known FM materials at different length scales. Exploitation of their dynamic responses over broad temporal and spatial regimes can offer various exciting properties. These magnetic nanostructures form the basis of future technologies including magneto-photonic crystals [2,3] and ultrahigh density storage devices. They also possess exciting prospects in the field of magnonics as magnonic crystals (MCs) [4] where spin waves (SWs) are used to carry and process the information in the microwave band analogous to photonic and phononic crystals. They can play a key role in building nanoscale magnonic devices for GHz-frequency communication [5], waveguides [6], phase shifters [7], filters [8], interferometers [9], SW logic devices [10], and SW nano-optics [11] with SWs in multiple connected magnon waveguides. More recently, the filled AD lattices have also gained great interest as

bicomponent MCs [5,12] (BMCs) for additional tunability in the magnonic band structures due to the differences between the magnetic parameters of two magnetic materials in those systems. The upsurge in the nanofabrication and detection techniques with improved spatio-temporal resolution boosts the study of high-frequency magnetization dynamics in a variety of nanoscale ADLs. One important problem in magnonics research is to tune the magnonic spectra and the band structures of the MCs by varying the physical parameters such as the shape [13], lattice symmetry [14,15], lattice constant [16], and base material [17], as well as the strength and orientation of the bias magnetic field [18,19], which can greatly affect the SW dynamics.

In the past few years, the high-frequency magnetization dynamics of magnetic ADLs have been explored by various experimental and numerical methods [18–23]. Initial studies on ADLs showed attenuation of a uniform FM resonance mode due to the excitation of a nonuniform in-plane SW mode [24] and the pattern-induced splitting of the surface and volume modes [25] was also observed. Later, field-dependent localization of SW mode, SW confinement, and field-controlled propagation of SWs [26,27]

*abarman@bose.res.in

as well as the formation of magnonic minibands with large SW velocities [28,29] were observed. Recently, the dispersive and entangled SWs between the ADs [30] and anisotropic propagation and damping of SWs [18] were also observed due to the magnetic-field-induced SW guiding in a network of interconnected nanowires. Further works showed high-symmetric magnonic modes having a linear bias magnetic field dependence for perpendicularly magnetized ADs [31], and conversion of quantized SWs to propagating ones by varying the bias magnetic field orientation [19]. Micromagnetic simulations reported [32] the effect of the AD shape on the magnonic band structure in exchange-dominated one-dimensional magnonic waveguides. The effects of lattice defects [33] and broken translational symmetry [34] have also attracted great interest due to their unique properties. However, there are very few reports exploring the effect of the size of the ADs [35], which can play a key role in determining the nature of SW propagation and confinement due to the modulation of the magnonic band gaps in such MCs.

Here, we investigate the SW dynamics of 2D arrays of circular-shaped $\text{Ni}_{80}\text{Fe}_{20}$ ADs arranged in hexagonal lattice with a fixed lattice constant but varying AD diameter by manipulating the strength and orientation of the in-plane bias magnetic field. A drastic variation in the magnonic spectra is observed when the diameter of the AD is systematically tuned. A rich band of SW modes for the highest AD diameter is systematically reduced to a fewer number of modes with the reduction in AD diameter. Further, a mode crossover with bias-field strength and a mode-hopping-like behavior with bias-field orientation are observed, which are explained with the aid of micromagnetic simulations.

II. SAMPLE FABRICATION AND EXPERIMENTAL TECHNIQUE

Circular-shaped ADs are patterned in a 20-nm-thick $\text{Ni}_{80}\text{Fe}_{20}$ (Ni-Fe) film by using a combination of *e*-beam lithography (EBL), *e*-beam evaporation (EBE), and ion milling [15]. The ADs with variable diameters (d) of 140 (D1), 240 (D2), 340 (D3), and 440 (D4) nm and a fixed lattice spacing (a) of 700 nm are arranged in a hexagonal lattice with total array dimensions of $25 \times 250 \mu\text{m}^2$, as shown in the scanning electron micrographs of Fig. 1(a). A co-planar waveguide (CPW) made of Au with a thickness of 150 nm is deposited on top of the array for the broadband ferromagnetic resonance (FMR) measurement. The width and length of the signal line of this CPW are 30 and $300 \mu\text{m}$, respectively, so that the whole array can remain under the center of the signal line of the CPW, which has a nominal characteristic impedance of 50Ω .

The measurement of SW spectra from the samples is performed using a broadband FMR spectrometer [36] consisting of a vector network analyzer (Agilent PNA-L, Model No.: N5230C, frequency range: 10 MHz–50 GHz) and a high-frequency probe station along with a nonmagnetic ground-signal-ground (GSG)-type picoprobe (GGB Industries, Model No. 40A-GSG-150-EDP). The system has a built-in electromagnet within the probe station generating a bias magnetic field (H_{ext}) of ± 1800 Oe. The electromagnet is mounted on a high-precision rotary mount, which enables the electromagnet to rotate over a 360° angle within the plane of the sample. The sample is viewed with the help of a microscope and illumination setup. A microwave signal with variable frequency is launched into the CPW using the picoprobe through a high-frequency and low-noise coaxial cable (Model No.: N1501A-203).

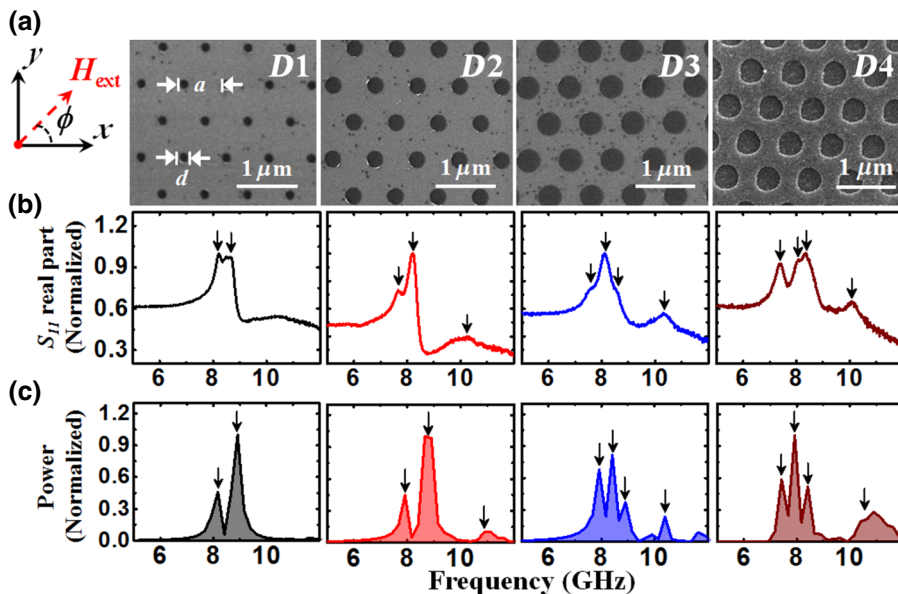


FIG. 1. (a) Scanning electron micrographs of circular-shaped $\text{Ni}_{80}\text{Fe}_{20}$ (Ni-Fe) ADs arranged in hexagonal lattices of constant lattice spacing $a = 700$ nm with variable AD (hole) diameter $d = 140$ (D1), 240 (D2), 340 (D3), and 440 (D4) nm. (b) Real parts of the forward scattering parameter (S_{11}) representing the FMR spectra for all four samples at a bias magnetic field $H_{\text{ext}} = 800$ Oe applied at an azimuthal angle $\phi = 0^\circ$. The observed SW modes are marked by down arrows. (c) Corresponding simulated SW spectra of four different lattices at $H_{\text{ext}} = 800$ Oe applied at $\phi = 0^\circ$ and the arrows represent different SW modes. The orientation of the bias magnetic field H_{ext} is shown at the top left of the figure.

The CPW is shorted at one end and the back-reflected signal is collected by the same probe to the analyzer. Absorption of the ongoing and returning signals at various SW frequencies produces the characteristic SW spectrum of the sample. The real and imaginary parts of the scattering parameter in reflection geometry measured at various magnetic fields are subtracted from its value at the maximum bias magnetic field (reference spectrum), and hence, the SW spectra are obtained (additional details about sample fabrication and experimental method can be found in [37]).

III. EXPERIMENTAL RESULTS AND MICROMAGNETIC SIMULATION

The real parts of the forward scattering parameter, i.e., S_{11} for the samples with varying AD diameter (d), are shown in Fig. 1(b) at a bias magnetic field of $H_{\text{ext}} = 800$ Oe applied at an azimuthal angle $\phi = 0^\circ$, while their bias field-dependent SW dispersion spectra measured at $\phi = 0^\circ$ are represented as surface plots in Fig. 2. The SW dynamics are drastically modified with the variation of d . For D1, two distinct SW modes are obtained, while in the case of D2, the number of modes is increased to three. On the contrary, rich multimode spectra are observed in D3 and D4 consisting of a total of six and eight modes. Interestingly, in D4, with the decreasing bias field, we observe a significant crossover (marked by the red dotted box in the field dispersion of D4 in Fig. 2) between the two higher-frequency branches (closed and open diamond-marked modes 7 and 8, respectively) at an intermediate field value of $H_{\text{ext}} \sim 525$ Oe. A crossover is also observed in D3 as shown by the black dotted box in Fig. 2 between modes

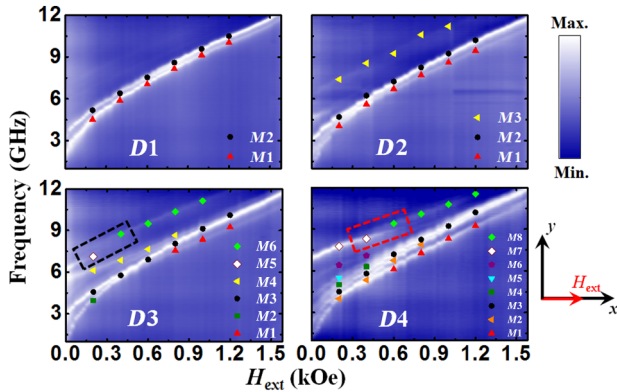


FIG. 2. Bias field (H_{ext})-dependent SW absorption spectra of Ni-Fe ADs with different AD diameters (D1–D4) are shown at $\phi = 0^\circ$. The surface plots correspond to the experimental results, while the symbols represent the simulated data. The black and red dotted boxes represent the crossover between two higher-frequency branches, i.e., M5 and M6 in D3 and M7 and M8 in D4, respectively. The color map for the surface plots and the schematic of H_{ext} are given at the right side of the figure.

5 and 6 (closed and open diamond-marked modes) at a much lower field $H_{\text{ext}} \sim 170$ Oe, while this phenomenon is completely absent in both D1 and D2. Also, the lowest frequency mode M1 in both D3 and D4 vanishes above a certain bias field value (approximately 700 Oe for D3 and approximately 430 Oe for D4). The bias field dispersion curves of D3 and D4 also reveal that there are some SW modes, e.g., M2 in D3 and M5 in D4, which are present at a lower bias field. This is due to the deviation from the uniform magnetization state due to the increase in the overlapping between the demagnetizing regions around the ADs.

We investigate the origin of the SW modes by performing micromagnetic simulations using the OOMMF software [38] for these samples consisting of 2×2 arrays of hexagonal unit cells for each sample where the two-dimensional (2D) periodic-boundary condition is incorporated to consider the large areas of the experimentally studied arrays. We discretize each sample into rectangular prismlike cells with dimensions of $4 \times 4 \times 20$ nm³. The values of exchange stiffness constant and saturation magnetization used in the simulation for Ni-Fe are $A_{\text{Ni-Fe}} = 1.3 \times 10^{-6}$ erg/cm [39] and $M_{\text{Ni-Fe}} = 850$ emu/cm³, respectively, while the damping coefficient $\alpha_{\text{Ni-Fe}} = 0.008$ is used for Ni-Fe during the dynamic simulations. The values of the gyromagnetic ratio $\gamma = 18.1$ MHz/Oe and the magnetocrystalline anisotropy $K = 0$ are considered for Ni-Fe. Here, the material parameters, i.e., M_s , γ , and K for Ni-Fe, are extracted from the Kittel fit of the bias-field-dependent SW absorption spectra of the Ni-Fe thin film (Fig. S1 [37]). The dynamic simulations are carried out by first performing a static magnetic configuration under a bias magnetic field in the experimental geometry and then by applying a pulsed magnetic field. The details of the static and the dynamic simulations are described elsewhere [40].

Figure 1(c) shows that the experimental data are qualitatively well reproduced using the micromagnetic simulations, which are plotted at $H_{\text{ext}} = 800$ Oe, and also in Fig. 2 as represented by filled symbols for all the lattices. The slight quantitative disagreements between experimental and simulated results can occur due to the deviation of the simulated samples and conditions from the experimental ones. The general deviation in the dimensions as observed in the experimental samples has already been incorporated in the simulated samples, although the precise edge deformations are not possible to include in the finite-difference-method-based micromagnetic simulations.

In Fig. 3(a), we show the simulated static magnetic configurations for D1 and D2 at $H_{\text{ext}} = 800$ Oe ($\phi = 0^\circ$), while in order to underpin the origin of the mode crossover observed in both D3 and D4, we present their static magnetization states at two different bias field values, $H_{\text{ext}} = 200$ and 800 Oe. The static magnetization maps of D3 and D4 at $H_{\text{ext}} = 200$ Oe reveal a strong overlap of the demagnetized

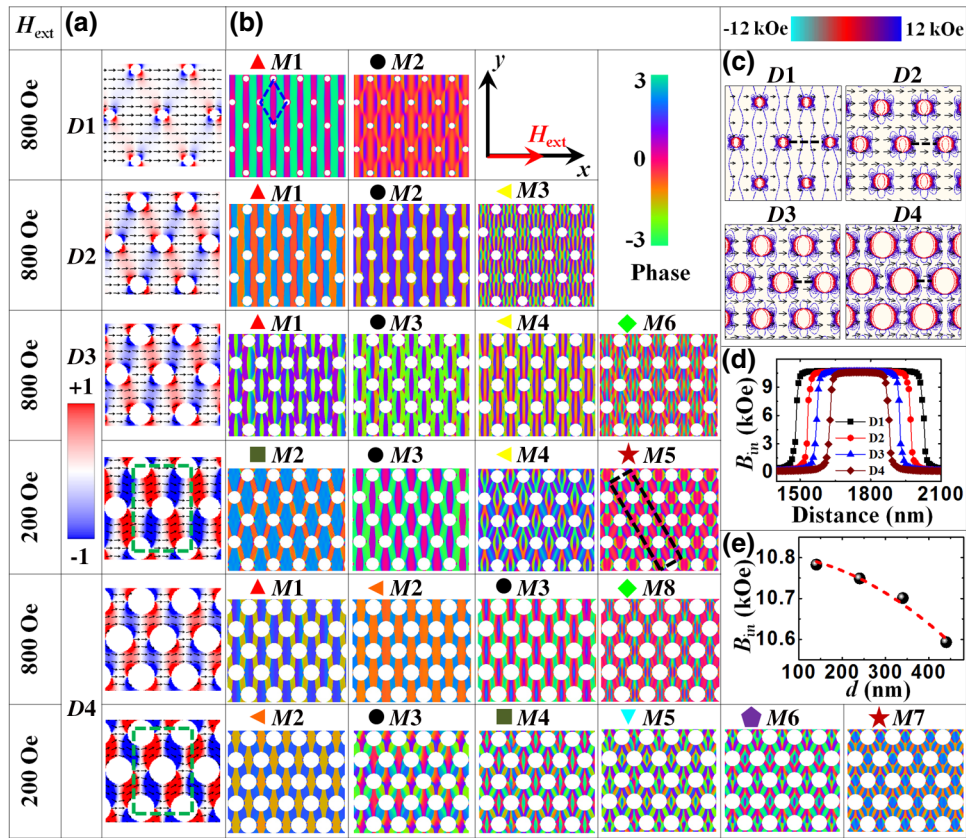


FIG. 3. (a) Simulated static magnetic configurations of Ni-Fe ADLs are shown for $H_{\text{ext}} = 800$ Oe in D1–D4 and $H_{\text{ext}} = 200$ Oe in D3 and D4, respectively, at $\phi = 0^\circ$. The color map is given on the left side of the figure. (b) Simulated spatial distributions of the phase profiles corresponding to different SW modes obtained at $H_{\text{ext}} = 800$ Oe in D1–D4 and $H_{\text{ext}} = 200$ Oe in D3 and D4, respectively, at $\phi = 0^\circ$. The color map for the phase distributions and the schematic of H_{ext} are shown on the right side of the figure. (c) Contour plots of the simulated magnetostatic field distributions in D1–D4. The corresponding color map is given at the top right corner of the figure. (d) Line scans of the simulated internal field (B_{in}) taken between two consecutive ADs along the black dotted lines as shown in (c) for D1–D4. (e) The variation of B_{in} with the AD diameter d (black circular symbols: micromagnetic symbols; red dotted line: fitted curve).

regions present between the two ADs situated diagonally (as shown by the green dotted boxes) of the lattices, while this overlap is systematically reduced with the increase in bias field and vanishes for $H_{\text{ext}} > 300$ Oe in D3 and $H_{\text{ext}} > 600$ Oe in D4, respectively. For a better understanding of the nature of the various observed SW modes, we calculate the spatial distributions of these SW modes using a homebuilt code [41]. Figure 3(b) shows the phase profiles (corresponding power profiles are shown in Fig. S2 [37]) of the SW modes for all samples with varying d , calculated at $H_{\text{ext}} = 800$ Oe for $\phi = 0^\circ$. We observe different types of extended and quantized standing-SW modes due to the formation of confining potentials by the demagnetizing fields around the ADs. Thus, in order to maintain uniformity in describing the nature of the observed standing-SW modes, we assign quantization number n for the modes forming standing waves in the rhombic region between the two (horizontally situated) consecutive ADs along the x direction, as shown by the blue dotted box in the phase profile

of M1 for D1. It is clear from Fig. 3(b) that the lowest frequency mode M1 for D1 is extended through the diagonally situated ADs along the y direction. However, considering the rhombic region formed by four ADs, it also forms a standing wave mode along the x direction with quantization $n = 3$, while the other mode M2 has a quantized character along the x direction with $n = 5$. Similarly, in D2, both lower-frequency modes M1 and M2 show an extended nature in the y direction. Although M1 and M2 also possess a quantized character along the x direction in the rhombic unit with $n = 3$, they are in opposite phases with each other. The highest frequency mode M3 of D2 also forms a standing wave pattern with $n = 11$. The mode profiles are substantially modified with a further increase in d , and the SWs form standing waves in the x direction for D3 and D4. However, unlike for D1 and D2, some of the SW modes show discontinuity for low- or high-field values in D3 and D4. To explain this, we have shown the phase maps of the SW modes, which are present at $H_{\text{ext}} = 200$

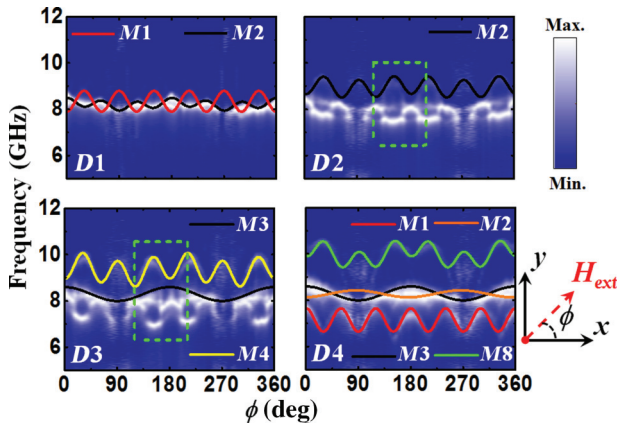


FIG. 4. Variation of SW frequency with the azimuthal angle (ϕ) varying from 0° to 360° for Ni-Fe ADLs with various AD diameters (D1–D4) at $H_{\text{ext}} = 800$ Oe. The surface plots represent the experimental results while the solid lines describe the sinusoidal fits to the observed anisotropic SW modes in all of the samples (D1–D4). The color maps associated with the surface plots and the schematic of the orientation of H_{ext} are shown on the right side of the figure.

and 800 Oe for D3 and D4. For D3 at $H_{\text{ext}} = 800$ Oe, both M1 and M3 are quantized modes with $n = 3$, which are opposite in phase, while M4 and M6 also possess a quantized character with $n = 5$ and 7, respectively. However, at a lower bias field ($H_{\text{ext}} = 200$ Oe), M2 shows a quantized nature with $n = 1$. On the other hand, due to the increase in the overlapping of demagnetized regions as is evident from the static magnetization profile shown in Fig. 3(a) for D3, a diagonal quantization between the next nearest neighboring ADs is observed for M5 as shown by the black

dotted box. We assign m as the diagonal quantization number where $m = 3$ for M5. In D4, at $H_{\text{ext}} = 800$ Oe, all the modes (M1, M2, M3, and M8) have quantized natures with $n = 1, 1, 3, \text{ and } 5$, respectively, where M1 and M2 are in the opposite phases. However, at $H_{\text{ext}} = 200$ Oe, due to a strong demagnetizing field, a significant modification is observed where all the SW modes M2–M7 represent quantized modes with $n = 1, 3, 3, 3, 3, \text{ and } 1$, respectively, with their diagonal quantization values m of 1, 1, 3, 3, 5, and 5, respectively. Here, M4 and M5 are in opposite phases with each other.

We further calculate the magnetostatic field distributions in the ADLs for bias field $H_{\text{ext}} = 800$ Oe applied at $\phi = 0^\circ$ using the LLG software [42], as shown in Fig. 3(c). It can be clearly seen that the magnetostatic field distribution is modified drastically when d is varied. We further compare the internal field (B_{in}) values of these samples by taking a linescan between two consecutive ADs along the x direction as shown by the black dotted lines in D1–D4. It is found that B_{in} decreases significantly with the increase in d , due to the systematic increase in the overlapping between the demagnetizing fields confined around the ADs. This variation of B_{in} is fitted using a simple parabolic equation, which reflects that B_{in} varies with $-d^2$ in the following equation:

$$B_{\text{in}} = A(-d^2) + C, \quad (1)$$

where C is the B_{in} value (approximately 10.81 kOe) of the Ni-Fe thin film having a thickness of 20 nm. To confirm this behavior, we calculate the internal field values for additional simulated samples with $d = 40$ and 540 nm and the B_{in} values of these samples also follow the same fitting with Eq. (1) (see Fig. S3 [37]).

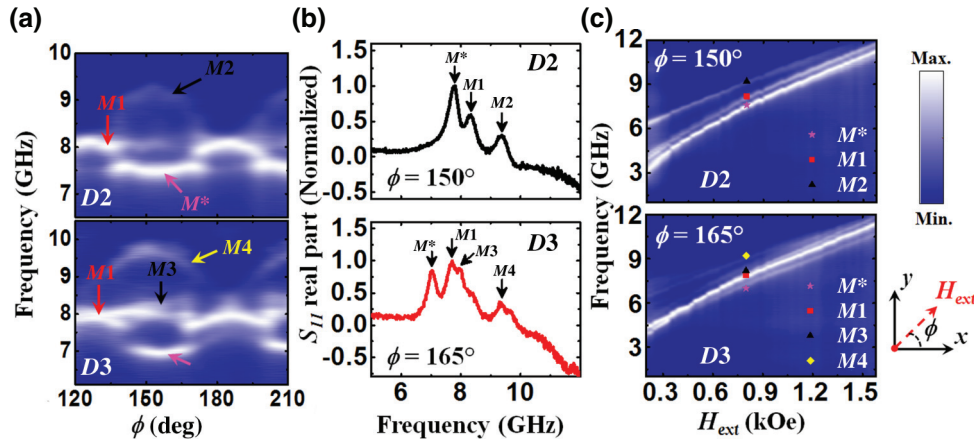


FIG. 5. (a) Angular dispersion of FMR spectra of D2 and D3 for $120^\circ \leq \phi \leq 210^\circ$ obtained from Fig. 4 as marked by green dotted boxes in D2 and D3. (b) Real parts of the forward scattering parameter (S_{11}) representing the FMR spectra for D2 and D3 at bias magnetic field $H_{\text{ext}} = 800$ Oe applied at azimuthal angles $\phi = 150^\circ$ and 165° , respectively. The observed SW modes are marked by down arrows. (c) Bias field (H_{ext})-dependent SW absorption spectra of D2 at $\phi = 150^\circ$ and D3 at $\phi = 165^\circ$ are shown with $H_{\text{ext}} = 800$ Oe. The surface plots correspond to the experimental results, while the symbols represent the simulated data. The color map for the surface plots and the schematic of H_{ext} are given on the right side of the figure.

To investigate the configurational anisotropy in these samples, we measure the SW spectra of these samples by varying the in-plane orientation (ϕ) of the bias magnetic field at a fixed strength. Figure 4 presents surface plots of the angular dispersion of SW frequencies for all the samples (D1–D4) at $H_{\text{ext}} = 800$ Oe. The solid lines represent the theoretical fits using harmonic functions with different rotational symmetries. The anisotropy of the SW modes vary significantly as d is increased. The lowest frequency mode M1 for D1 shows six-fold rotational anisotropy, while M2 possesses a superposition of strong six- and weak two-fold anisotropies. The higher-frequency anisotropic modes, i.e., M2 in D2 and M4 in D3, show a combination of six- and two-fold rotational symmetry. On the other hand, M1 and M8 in D4 also possess six-fold rotational symmetry along with a weak two-fold symmetry, although M8 is in opposite phase with M1. Additionally, a two-fold anisotropy is observed in D4 for the two intermediate SW modes M2 and M3, while they are in opposite phases with each other.

In contrast, the angular dispersions of the SW modes for D2 and D3 reflect very interesting behaviors as there

is a stark modulation in the SW intensity of M1 in both D2 and D3 when the bias field orientation is varied. This phenomenon is more prominent in Fig. 5(a), which has been extracted from Fig. 4, for $120^\circ \leq \phi \leq 210^\circ$, as marked by the green dotted boxes in D2 and D3, respectively. In D2, for $135^\circ \leq \phi \leq 165^\circ$, an apparent mode hopping occurs from mode M1 to a new mode M*. However, on a closer look, it appears that the mode splits into a higher power lower-frequency mode M*, while M1 also retains a very low power and M2 possesses a systematic dispersion. This multimodal oscillation for the limited angular range is similar to optical parametric generation, which appears and disappears periodically with an angular period of 60° . A similar behavior is observed for D3, but here, in addition to the two modes (M* and M4), another mode M3 remains very close to M1. The presence of this additional mode M* is also confirmed from the bias field-dependent SW dispersion curves of D2 and D3 measured at $\phi = 150^\circ$ and 165° , respectively, as demonstrated in Fig. 5(c). This behavior is reconfirmed by the SW spectra shown in Figs. 1(b) and 5(b), which show the appearance and disappearance of the additional modes with M1 at a regular interval of 60° .

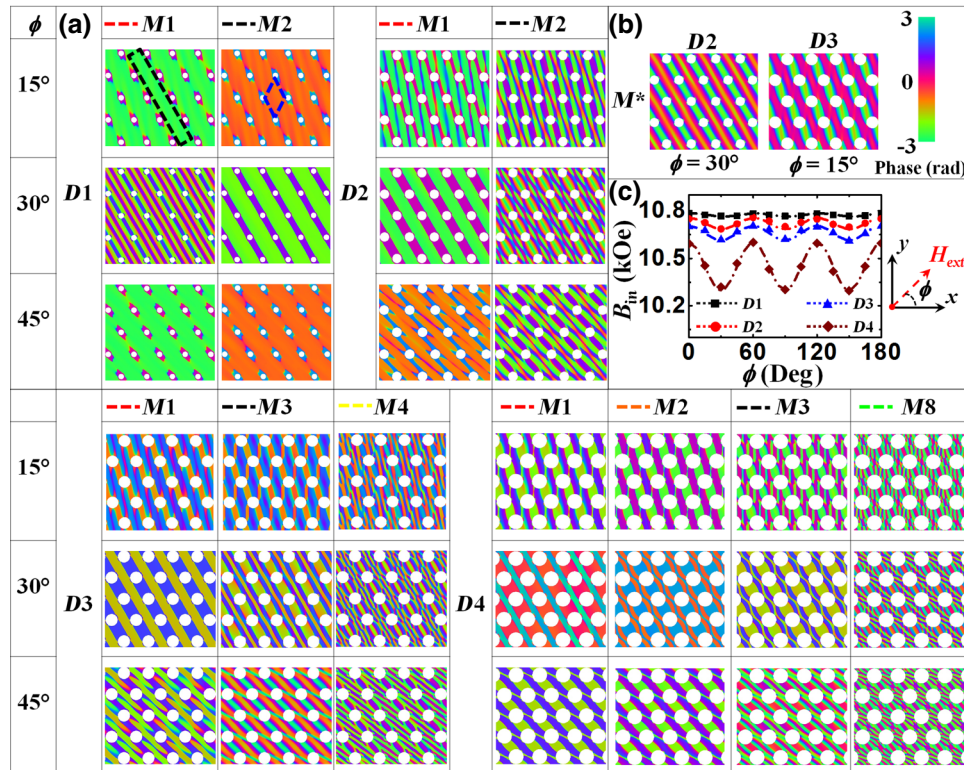


FIG. 6. (a) Simulated spatial distributions of the phase profile corresponding to different anisotropic SW modes obtained in D1–D4 with $H_{\text{ext}} = 800$ Oe at $\phi = 0^\circ, 15^\circ, 30^\circ$, respectively. The black dotted box inside mode 1 (M1) of D1 at $\phi = 15^\circ$ represents the nature of the extended SW mode in a direction perpendicular to H_{ext} . (b) Simulated phase maps of the additional SW mode (M*) obtained in D2 at $\phi = 30^\circ$ and D3 at $\phi = 15^\circ$, respectively, with $H_{\text{ext}} = 800$ Oe. The color map for the phase distributions and the schematic of H_{ext} are shown on the top right corner of the figure. (c) Evolution of the simulated internal field (B_{in}) values in D1–D4 with varying ϕ at $H_{\text{ext}} = 800$ Oe obtained by taking line scans in the region marked by the blue dotted box inside mode 2 (M2) of D1 at $\phi = 15^\circ$.

The evolution of SW phase maps (corresponding power maps are shown in Fig. S4 [37]) with ϕ in Fig. 6(a) shows that mode M1 in D1 remains almost invariant, i.e., extended in the direction perpendicular to the bias field along the Ni-Fe channel between the ADs as marked by the black dotted box in M1 of D1. The quantization along the field direction is modified when ϕ is changed from 0° to 30° . However, M2 is converted into an extended mode from a quantized mode when ϕ is rotated from 0° to 15° or more. On the other hand, both the SW modes (M1 and M2) in D2 experience a significant transformation as ϕ changes to 30° and are converted to the extended modes inside the Ni-Fe channel, but with different quantization numbers along the field direction. Similarly, in D3, when ϕ is increased, the two lower-frequency anisotropic modes M1 and M3 undergo conversion from quantized SW modes to extended modes, but with different quantization numbers inside the Ni-Fe channel, whereas M4 remains spatially invariant with ϕ . The asterisk marked mode M* in D2 shows an extended nature at $\phi = 30^\circ$, while in D3 it represents quantized behavior at $\phi = 15^\circ$ similar to M1, although they are in opposite phases with each other as evident from Figs. 6(a) and 6(b). Interestingly, the lowest frequency mode M1 in D4 becomes an extended mode at $\phi = 30^\circ$ and again becomes a quantized mode when ϕ is increased to 45° , but the other anisotropic modes M2, M3, and M8 remain almost unaltered with the variation of ϕ . The origin of the observed two-fold rotational anisotropy can be explained by considering the boundary effect coming from the rectangular shape of the boundary of the samples, which has been confirmed from the angular dispersion spectra of the Ni-Fe thin film measured at $H_{\text{ext}} = 800$ Oe (see Fig. S5 [37]). To unravel the reason behind the presence of the six-fold anisotropic behavior observed in all the lattices, the variation of the internal field (B_{in}) for D1–D4 is calculated at various orientations of the bias field by keeping its strength fixed to $H_{\text{ext}} = 800$ Oe in the region marked by the blue dotted box as shown in M2 of D1 at $\phi = 15^\circ$ in Fig. 6(a). It is evident from Fig. 6(c) that the variation of B_{in} with ϕ indeed possesses a periodic six-fold rotational symmetry in the case of all the samples, where this anisotropic contribution increases systematically from D1 to D4. Consequently, this is reflected as the anisotropic behavior of the SW-mode frequencies in the angular dispersion behavior obtained for these lattices.

IV. CONCLUSION

In summary, we have investigated the evolution of magnetization dynamics of hexagonally arranged Ni-Fe circular AD arrays with varying AD diameters having same lattice spacing by controlling the bias magnetic field strength and its in-plane orientation using a broadband

FMR technique. The field dispersion spectra of these systems reveal that the SW dynamics are drastically modified as the AD diameter is varied. Rich multimodal SW spectra are obtained for the highest AD diameter, whereas the number of SW modes reduces systematically with the decreasing AD diameter. Moreover, a crossover between two higher-frequency SW modes is observed for the lattices with higher hole diameters when the strength of the bias field is reduced. The simulated static magnetic configurations along with the power and phase profiles unravel the spatial distribution of the observed SW modes, which confirms the formation of SW quantization laterally as well as diagonally inside the array having higher hole diameters at a low bias field due to the strong overlapping of demagnetization regions between the ADs. As a result, the internal field is significantly reduced with the enhancement in AD diameter. The variation of magnonic spectra with the in-plane orientation for all the samples shows the presence of two anisotropic SW modes, both in opposite phase to each other, with six-fold rotational symmetry, which is strongly modulated when the hole diameter is increased. Interestingly, for intermediate AD diameters, the lowest frequency SW mode apparently shows a mode-hopping-like behavior with 60° periodicity, but a closer look reveals a parametric splitting of the mode. The phase maps of these samples unveil an interesting conversion from an extended nature to a quantized standing-wave pattern or vice-versa in most of these anisotropic SW modes with the modulation of in-plane orientation. Further, the variation of the internal field with the in-plane orientation confirms the presence of six-fold anisotropy, which is strongly modulated when the diameter of the ADs is modified. Thus, the variation in both the AD size and the magnetic field orientation demonstrate active methods essentially leading to a modulation in the profile of a periodically varying SW channel, which may subsequently determine the SW frequency dispersion. This property can be implemented in dynamic SW filters and magnonic waveguides in the GHz-frequency range. Also, the observed mode-hopping-like behavior can be utilized in nonlinear magnonic devices or coupled waveguides analogous to opto-electronic devices in photonics. Therefore, the observed tunability of the magnetization dynamics with the AD size as well as the strength and orientation of the in-plane bias field plays a crucial role from a fundamental scientific viewpoint as well as in terms of the nanoscale magnonic crystal-based technology.

ACKNOWLEDGMENTS

The authors gratefully acknowledge financial support from the Department of Science and Technology, Government of India under Grant No. SR/NM/NS-09/2011 and S. N. Bose National Centre for Basic Sciences for Grant No. SNB/AB/12-13/96 and SNB/AB/18-19/211.

S.C. acknowledges S. N. Bose National Centre for Basic Sciences for financial assistance.

-
- [1] S. Neusser and D. Grundler, Magnonics: Spin waves on the nanoscale, *Adv. Mater.* **21**, 2927 (2009).
- [2] G. Ctistis, E. Papaioannou, P. Patoka, J. Gutek, P. Fumagalli, and M. Giersig, Optical and magnetic properties of hexagonal arrays of subwavelength holes in optically thin cobalt films, *Nano Lett.* **9**, 1 (2009).
- [3] K. Kern, D. Heitmann, P. Grambow, Y. H. Zhang, and K. Ploog, Collective Excitations in Antidots, *Phys. Rev. Lett.* **66**, 1618 (1991).
- [4] V. V. Kruglyak, S. O. Demokritov, and D. Grundler, Magnonics, *J. Phys. D: Appl. Phys.* **43**, 264001 (2010).
- [5] H. Yu, G. Duerr, R. Huber, M. Bahr, T. Schwarze, F. Brandl, and D. Grundler, Omnidirectional spin-wave nanograting coupler, *Nat. Commun.* **4**, 2702 (2013).
- [6] V. V. Kruglyak, A. Barman, R. J. Hicken, J. R. Childress, and J. A. Katine, Picosecond magnetization dynamics in nanomagnets: Crossover to nonuniform precession, *Phys. Rev. B* **71**, 220409(R) (2005).
- [7] Y. Au, M. Dvornik, O. Dmytriiev, and V. V. Kruglyak, Nanoscale spin wave valve and phase shifter, *Appl. Phys. Lett.* **100**, 172408 (2012).
- [8] S. K. Kim, K. S. Lee, and D. S. Han, A gigahertz-range spin-wave filter composed of width-modulated nanostrip magnonic-crystal waveguides, *Appl. Phys. Lett.* **95**, 082507 (2009).
- [9] J. Podbielski, F. Giesen, and D. Grundler, Spin-Wave Interference in Microscopic Rings, *Phys. Rev. Lett.* **96**, 167207 (2006).
- [10] M. Jamali, J. H. Kwon, S.-M. Seo, K.-J. Lee, and H. Yang, Spin wave nonreciprocity for logic device applications, *Sci. Rep.* **3**, 3160 (2013).
- [11] V. E. Demidov, S. O. Demokritov, K. Rott, P. Krzyszczo, and G. Reiss, Nano-optics with spin waves at microwave frequencies, *Appl. Phys. Lett.* **92**, 232503 (2008).
- [12] S. Choudhury, S. Saha, R. Mandal, S. Barman, Y. Otani, and A. Barman, Shape- and interface-induced control of spin dynamics of two-dimensional bicomponent magnonic crystals, *ACS Appl. Mater. Interfaces* **8**, 18339 (2016).
- [13] R. Mandal, P. Laha, K. Das, S. Saha, S. Barman, A. K. Raychaudhuri, and A. Barman, Effects of antidot shape on the spin wave spectra of two-dimensional $\text{Ni}_{80}\text{Fe}_{20}$ antidot lattices, *Appl. Phys. Lett.* **103**, 262410 (2013).
- [14] S. Tacchi, M. Madami, G. Gubbiotti, G. Carlotti, A. O. Adeyeye, S. Neusser, B. Botters, and D. Grundler, Angular dependence of magnetic normal modes in NiFe antidot lattices with different lattice symmetry, *IEEE Trans. Magn.* **46**, 1440 (2010).
- [15] R. Mandal, S. Barman, S. Saha, Y. Otani, and A. Barman, Tunable spin wave spectra in two-dimensional $\text{Ni}_{80}\text{Fe}_{20}$ antidot lattices with varying lattice symmetry, *J. Appl. Phys.* **118**, 053910 (2015).
- [16] R. Mandal, S. Saha, D. Kumar, S. Barman, S. Pal, K. Das, A. K. Raychaudhuri, Y. Fukuma, Y. Otani, and A. Barman, Optically induced tunable magnetization dynamics in nanoscale co antidot lattices, *ACS Nano* **6**, 3397 (2012).
- [17] S. Pal, J. W. Klos, K. Das, O. Hellwig, P. Gruszecki, M. Krawczyk, and A. Barman, Optically induced spin wave dynamics in [co/pd]8 antidot lattices with perpendicular magnetic anisotropy, *Appl. Phys. Lett.* **105**, 162408 (2014).
- [18] S. Neusser, G. Duerr, H. G. Bauer, S. Tacchi, M. Madami, G. Woltersdorf, G. Gubbiotti, C. H. Back, and D. Grundler, Anisotropic Propagation and Damping of Spin Waves in a Nanopatterned Antidot Lattice, *Phys. Rev. Lett.* **105**, 067208 (2010).
- [19] S. Tacchi, B. Botters, M. Madami, J. W. Klos, M. L. Sokolovskyy, M. Krawczyk, G. Gubbiotti, G. Carlotti, A. O. Adeyeye, S. Neusser, and D. Grundler, Mode conversion from quantized to propagating spin waves in a rhombic antidot lattice supporting spin wave nanochannels, *Phys. Rev. B* **86**, 014417 (2012).
- [20] B. Rana, D. Kumar, S. Barman, S. Pal, Y. Fukuma, Y. Otani, and A. Barman, Detection of picosecond magnetization dynamics of 50 nm magnetic dots down to the single dot regime, *ACS Nano* **5**, 9559 (2011).
- [21] W. J. Hsueh, C. H. Chen, and R. Z. Qiu, Perfect transmission of spin waves in a one-dimensional magnonic quasicrystal, *Phys. Lett. A* **377**, 1378 (2013).
- [22] V. N. Krivoruchko and A. I. Marchenko, Apparent sixfold configurational anisotropy and spatial confinement of ferromagnetic resonances in hexagonal magnetic antidot lattices, *J. Appl. Phys.* **109**, 083912 (2011).
- [23] M. Krawczyk, S. Mamica, M. Mruczkiewicz, J. W. Klos, S. Tacchi, M. Madami, G. Gubbiotti, G. Duerr, and D. Grundler, Magnonic band structures in two-dimensional bi-component magnonic crystals with in-plane magnetization, *J. Phys. D: Appl. Phys.* **46**, 495003 (2013).
- [24] O. N. Martyanov, V. F. Yudanov, R. N. Lee, S. A. Nepijko, H. J. Elmers, R. Hertel, C. M. Schneider, and G. Schön-hense, Ferromagnetic resonance study of thin film antidot arrays: Experiment and micromagnetic simulations, *Phys. Rev. B* **75**, 174429 (2007).
- [25] S. McPhail, C. M. Gürtler, J. M. Shilton, N. J. Curson, and J. A. C. Bland, Coupling of spin-wave modes in extended ferromagnetic thin film antidot arrays, *Phys. Rev. B* **72**, 094414 (2005).
- [26] S. Neusser, B. Botters, and D. Grundler, Localization, confinement, and field-controlled propagation of spin waves in $\text{Ni}_{80}\text{Fe}_{20}$ antidot lattices, *Phys. Rev. B* **78**, 054406 (2008).
- [27] S. Neusser, B. Botters, M. Becherer, D. Schmitt-Landsiedel, and D. Grundler, Spin-wave localization between nearest and next-nearest neighboring holes in an antidot lattice, *Appl. Phys. Lett.* **93**, 122501 (2008).
- [28] R. Zivieri, S. Tacchi, F. Montoncello, L. Giovannini, F. Nizzoli, M. Madami, G. Gubbiotti, G. Carlotti, S. Neusser, G. Duerr, and D. Grundler, Bragg diffraction of spin waves from a two-dimensional antidot lattice, *Phys. Rev. B* **85**, 012403 (2012).
- [29] S. Neusser, G. Duerr, S. Tacchi, M. Madami, M. L. Sokolovskyy, G. Gubbiotti, M. Krawczyk, and D. Grundler, Magnonic minibands in antidot lattices with large spin-wave propagation velocities, *Phys. Rev. B* **84**, 094454 (2011).
- [30] M. Kostylev, G. Gubbiotti, G. Carlotti, G. Socino, S. Tacchi, C. Wang, N. Singh, A. O. Adeyeye, and R. L. Stamps,

- Propagating volume and localized spin wave modes on a lattice of circular magnetic antidots, *J. Appl. Phys.* **103**, 07C507 (2008).
- [31] R. Bali, M. Kostylev, D. Tripathy, A. O. Adeyeye, and S. Samarin, High-symmetry magnonic modes in antidot lattices magnetized perpendicular to the lattice plane, *Phys. Rev. B* **85**, 104414 (2012).
- [32] D. Kumar, P. Sabareesan, W. Wang, H. Fangohr, and A. Barman, Effect of hole shape on spin-wave band structure in one-dimensional magnonic antidot waveguide, *J. Appl. Phys.* **114**, 023910 (2013).
- [33] A. Manzin, G. Barrera, F. Celegato, M. Coisson, and P. Tiberto, Influence of lattice defects on the ferromagnetic resonance behaviour of 2d magnonic crystals, *Sci. Rep.* **6**, 22004 (2016).
- [34] S. Choudhury, S. Barman, Y. Otani, and A. Barman, Efficient modulation of spin waves in two-dimensional octagonal magnonic crystal, *ACS Nano* **11**, 8814 (2017).
- [35] J. Ding, D. Tripathy, and A. O. Adeyeye, Effect of antidot diameter on the dynamic response of nanoscale antidot arrays, *J. Appl. Phys.* **109**, 07D304 (2011).
- [36] B. K. Mahato, S. Choudhury, R. Mandal, S. Barman, Y. Otani, and A. Barman, Tunable configurational anisotropy in collective magnetization dynamics of $\text{Ni}_{80}\text{Fe}_{20}$ nanodot arrays with varying dot shapes, *J. Appl. Phys.* **117**, 213909 (2015).
- [37] See Supplemental Material at <http://link.aps.org/supplemental/10.1103/PhysRevApplied.10.064044> for (a) sample fabrication and experimental method, (b) bias-field-dependent SW absorption spectra for Ni-Fe thin films, (c) simulated spatial distribution power profiles corresponding to different SW modes in Ni-Fe antidot lattices, (d) simulated magnetostatic field distributions in Ni-Fe antidot lattices, (e) simulated spatial distribution power profiles corresponding to different SW modes at various in-plane orientations of the magnetic field, and (f) azimuthal angle-dependent SW absorption spectra for Ni-Fe thin films.
- [38] M. Donahue and D. G. Porter, *Oomf user's guide, version 1.0* (NIST Interagency Report No. 6376; National Institute of Standard and Technology, Gaithersburg, MD, 1999), URL: <http://math.nist.gov/oommf>.
- [39] K. H. J. Buschow, *Handbook of magnetic materials* (Elsevier, North Holland, Amsterdam, The Netherlands, 2009), Vol. 18, p. 168.
- [40] A. Barman and S. Barman, Dynamic dephasing of magnetization precession in arrays of thin magnetic elements, *Phys. Rev. B* **79**, 144415 (2009).
- [41] D. Kumar, O. Dmytriiev, S. Ponraj, and A. Barman, Numerical calculation of spin wave dispersions in magnetic nanostructures, *J. Phys. D: Appl. Phys.* **45**, 015001 (2012).
- [42] LLG micromagnetics simulator, <http://llgmicro.home.mindspring.com/>.